Improving the performances of supported NiCo catalyst for reforming of methane powered by magnetic induction

Violetta Poletto Dotsenko [a,c], Mariangela Bellusci [a], Andrea Masi [b], Daniela Pietrogiacomi [c], Francesca Varsano [a,*]

[a] *ENEA C.R. Casaccia, Via Anguillarese 301, 00123 Roma, Italy*
[b] *ENEA C.R. Frascati, Via E. Fermi 45, 00044 Frascati, RM, Italy*
[c] *University of Rome Sapienza, P.le A. Moro 5, 00185 Roma, Italy*

ARTICLE INFO

ABSTRACT

NiCo supported magnetic nanoparticles can catalyze the steam reforming of methane and at the same time provide the heat necessary to run the process by dissipating an external radio frequency electromagnetic field. Magnetic samples with different Ni:Co molar ratio and total metal loading on the support have been synthesized using a traditional impregnation procedure and characterized in terms of morphological and structural properties. The ability of the materials to provide process heat was assessed by temperature measurements. Methane conversion value and syngas composition have been measured for different applied field amplitude. The sample with a composition $Ni_{50}Co_{50}\_30$ wt% was found to be the most performing in terms of conversion obtained with the same applied magnetic field. The developed magnetic catalysts contribute to the transition to distributed hydrogen production and help to tackle some of the challenges related to the intensification of production processes by electrification.

1. Introduction

Electrification of chemical processes and reactors is one way that leads to intensification of industrial plant and it is currently being explored by the chemical industry to improve energy efficiency and reduce greenhouse gas emissions [1–5]. Electrification in the chemical industry can be applied to directly drive chemical reactions (typically electrochemical synthesis of chemical compounds) or to provide heating for thermal processes by direct Joule heating of the reactor or of the catalyst support [6–10]. The possibility of using contactless methods of transferring energy like microwave systems has been recently demonstrated [11–15]. They offer more-efficient process heating since the catalyst is directly heated to the reforming temperature, reduce carbon emissions and allow the construction of more compact reactor size, a particularly efficient technology but which however has shown scale up problems. More recently, the possibility of using radio frequency (r. f.) electromagnetic induction technology has been proposed to provide process heat at medium and high temperatures [16–29]. In particular, induction is coupled to the use of magnetic catalysts, materials which at the same time are able to catalyze the chemical process of interest and

provide the energy necessary to support it in an efficient and targeted way, interacting with the applied electromagnetic field. The proposed technology is highly innovative and has numerous and substantial advantages over traditional heating methods: (i) selective heating of the catalyst with resulting improvement of energy and chemical efficiency of the process, (ii) greatly reduced heat transfer limitations; (iii) almost instant heating (ramp rate >300–400 °C/min) which allows the possibility of feeding discontinuous and semi-continuous processes with rapid and efficient production cycles, thus limiting onerous and inefficient heat recovery systems; (iv) possibility of coupling chemical processes to renewable energy sources in emerging applications (e. g. Power to Chemicals / Power to Gas). The application of magnetic catalysis would therefore allow the implementation of highly energy-intensive processes on a small scale in an economical way. This implies overcoming the paradigm of large plants and is fully part of the development model aimed at decentralizing the production of chemical products, also using raw materials and renewable energy sources.

Eventually, thanks to the high safety, efficiency and speed of heating, r. f. electromagnetic induction has already conquered various industrial production sectors, particularly in the metallurgical field (brazing,

welding, sealing, casting, etc.) and the availability of radio frequency generators of different sizes (up to 1 MW) is guaranteed by various manufacturers. It is therefore reasonable to assume, once the technology has been validated, a rapid technology transfer.

In a recent paper [30] the authors reported the synthesis of NiCo nanoparticles supported on commercial γ-alumina pellets (NiCo/γ-Al$_2$O$_3$) behaving as efficient magnetic catalysts for the steam reforming of methane powered by induction. Samples with an alloy composition Ni$_{60}$Co$_{40}$ and two different loadings (17% and 30%) were prepared varying the synthesis process parameters. In that paper the effect of nanoparticles diameter on the heating capability of the material and hence on the conversion efficiency was highlighted.

In this work we explore the possibility of improving the NiCo/γ-Al$_2$O$_3$ catalyst performance through two different approaches, both aimed at obtaining higher working temperatures with the same applied field. In the first approach we increase the loading of the metal on the support (from 30% to 35% by weight) thus increasing the number of centers of energy dissipation. In the second one the cobalt content in the alloy is increased from 40 to 50 by mol. In fact cobalt, with respect to nickel, ensures a larger magnetic anisotropy, and thus better induction heating performance by hysteretic dissipation and, most importantly, a higher Curie temperature, Tc, (Tc is 1131 °C for Co and only 358 °C for Ni). Thus, the Tc is expected to increase from 780 °C (for Ni$_{60}$Co$_{40}$) to 850 °C (for Ni$_{50}$Co$_{50}$) [31,32].

2. Experimental

2.1. Catalysts synthesis

Supported NiCo catalyst nanoparticles are obtained by a conventional impregnation process from solution. Batches of 200 granules of γ-Al$_2$O$_3$ (form Alfa Aesar) as cylindrical (1/8″) pellets (specific surface area 250 m^{2}g^{-1}) are stirred overnight in a solution containing Ni(NO$_3$)$_2$ * 6 H$_2$O (Merck-EMSURE) and Co(NO$_3$)$_2$ * 6 H$_2$O (Merck-EMSURE) in different relative molar ratio (60:40 or 50:50) and total concentration (8 or 10 M). Recovered samples are dried at 80 °C and subsequently subjected to a calcination process in air flow. All the samples have been reduced in Ar-H$_2$ (3%vol) flow at 900 °C (heating ramp 10 °C/min) for 5 h. Molar composition of produced samples has been verified by Atomic Absorption Spectroscopy (AAS) utilizing a Varian Spectra AA-220.

In Table 1 significant parameters summarizing synthesis conditions and metal content of supported samples are reported. Samples are named on the basis of the expected molar composition and total metal weight.

2.2. Catalyst characterization

X-ray diffraction (XRD) analysis of the catalysts was performed on powders (pellets are easily grinded in a mortar) using a diffractometer equipped with a 120° linear simultaneous detector from INEL and a monochromatized Fe K$_{\alpha1}$ source.

Temperature Programmed Reduction (TPR) measurements have been recorded in a Micromeritics Autochem II 2920 apparatus. Measurements have been carried out on two granules (approximately 40 mg) to avoid observing a shift in the peak caused by mass effect.

The morphology of the catalyst pellets has been investigated by Scanning Electron Microscopy (SEM) using a high-resolution

microscope HRSEM LEO130. Measurements were performed after cleaving the sample into several pieces to investigate the morphology at the center of the pellet. To highlight the presence of the metallic phase dispersed on the alumina substrate, images were collected using a RBSD (backscatter) detector. To gain information on metal particle size and its distribution SEM images were processed by ImageJ software [33]. Size distribution histograms were fitted using a lognormal distribution function and evaluated Median particles diameters are reported.

Nitrogen adsorption measurements at 77 K were routinely executed with a Quantachrome NOVA 2200 apparatus and specific surface area of the samples was evaluated applying the BET method.

2.3. SAR evaluation and Induction setup for catalytic measurements

The capability of the magnetic samples to dissipate energy in the alternating r. f. field was evaluated under the following measurement conditions. About 5 g of catalyst were inserted inside the quartz reactor and subjected to magnetic fields of different intensity under a 100 mL/min nitrogen flow. Under these conditions, temperature profiles during heating and natural cooling in the absence of a field were recorded. From the analysis of these curves using the well-described procedure [34,35] summarized in SI the SAR (specific absorption rate) was evaluated (see Fig. S1). Such parameter, the absorbed power per unit mass, defines the heating performances of the magnetic nanoparticles.

We are aware that this measurement provides an estimation of the SAR and that magnetic measurements would be desirable to have more accurate data. Despite this, the data evaluated indirectly with this methodology provide interesting information on the behavior of the materials in operating conditions. To verify the accuracy of the methodology a sample was subjected to the same procedure utilizing two different inductor coils. The calculated SAR, reported and discussed in Supporting Information, is independent from the measurement setup within the estimated error.

The experimental setup utilized for determining the Ni-Co catalytic activity in the steam reforming reaction is schematized in [30]. Briefly, an Ambrell EasyHeat 2.4 induction apparatus has been utilized to heat the magnetic samples. The heating module (work head) is connected by r. f. cables to the power supply, allowing an easy positioning of the coil around the reactor. The apparatus can deliver a maximum power of 2 kW and operates in the 150–450 kHz frequency range. In this experimental campaign a 9-turn inductor coil of 5 cm diameter and 4.5 cm high, working at 242 kHz, is utilized; the field strength was estimated by the intensity of the current in the coils. An optic pyrometer (IRtech Radiamatic IR20CF2150) has been utilized for the estimation of the sample temperature. The pyrometer is focused on the surface of a pellet positioned at the external part of the reactor, where energy losses are more significant. It is reasonable to deduce that pellets positioned at the centre of the reactor may experience a higher temperature. Furthermore, it may happen that hot spots on the surface of the magnetic nanoparticles occur [36,37].

A mixture of water vapour and methane (always in the ratio 2:1, balanced with N$_2$) are conveyed to the reactor by a Vapour Delivery Module (VDM) (Bronkhorst). Gas Hourly Space Velocity (GHSV) values reported in the text are calculated on the basis of the geometrical volume occupied by catalyst pellets. To avoid water condensation, the lines connecting the VDM to the reactor are heated at 110 °C by Omegalux rope heaters. For the same reason, the quartz reactor is placed inside an

Table 1
Synthesis conditions and metal content of prepared catalysts.

Sample	Solution concentration	Calcination temperature (°C)/time (h)	Reduction temperature (°C)/time (h)	Expected %wt Me	Measured %wt Ni	Measured %wt Co
Ni$_{60}$Co$_{40}$_30	8 M	600/1	900/5	30	18.2 ± 0.8	11.7 ± 0.6
Ni$_{60}$Co$_{40}$_35	10 M	600/1	900/5	35	21.0 ± 0.9	14.3 ± 0.7
Ni$_{50}$Co$_{50}$_30	8 M	600/1	900/5	30	14.6 ± 0.6	15.3 ± 0.7

air-heated box (110 °C) thus avoiding the reflux of water. Two traps in series condense un-reacted water to prevent it from reaching the gas chromatograph, an Agilent GC490 equipped with two independent columns (MS5A and Plot-U) where the composition of reactant and product gas mixtures is analysed.

The conversion of methane X_{CH4} is calculated by the equation:

$$X_{CH4} = 100 * \frac{F_{tot}^{in} * CH_4^{in} - F_{tot}^{out} * CH_4^{out}}{F_{tot}^{in} * CH_4^{in}}$$

where F_{tot}^{in} is the total inlet flow, F_{tot}^{out} is the total outlet flow; CH_4^{in} and CH_4^{out} are the inlet and outlet volume fraction measured by the gas chromatograph.

3. Results and discussion

From the diffraction patterns reported in Fig. 1 it is possible to observe that the three materials consist of a Nickel-Cobalt alloy (as determined by comparison with ICCD-JCPDS database cards (4−850, 15−806) supported on alumina. The average size of the crystallites, according to the Debye-Sherrer formula and reported in Table 2.

The reducibility of bimetallic catalyst samples has been investigated by TPR measurement reported in Fig. 2. The profiles of the two $Ni_{60}Co_{40}$ and $Ni_{50}Co_{50}$ samples do not show dramatic difference. The low temperature peak, attributed to the reduction of Co_3O_4 to CoO shifts slightly from 335 °C to 363 °C at increasing cobalt content and the hydrogen consumption between 400 °C and 700 °C seems unaffected. In this temperature range both Co(II) to Co(0) and Ni(II) to Ni(0) reduction take place. The high temperature peak, usually attributed too to nickel reduction, shifts from 730 °C to 830 °C at increasing cobalt content. Such difference may be attributed to the different mean particle size of the alloy that grows from ~20nmfor $Ni_{60}Co_{40}$ sample to ~40 nm for $Ni_{50}Co_{50}$ (see Table 2) [38–41] as smaller nanoparticles are usually more readily reduced. In both cases the reduction does not conclude at 900 °C and an isothermal treatment was necessary to completely reduce the samples. Hydrogen consumed well matches the amount of loaded metals in both cases. The hydrogen consumption of a sample loaded with only cobalt and calcined according to the same procedure is reported in supporting information (Fig. S2) for an appropriate comparison. The main noticeable difference concerns the reducibility of cobalt, which is favored in mixed samples.

The nitrogen adsorption/desorption isotherm at 77 K is reported in Fig. 3 for $Ni_{60}Co_{40}$_35sample, illustrative for the different samples prepared. The isotherm presents essentially the substrate features, in fact all the prepared samples exhibit a type-IV (IUPAC) shape typical of
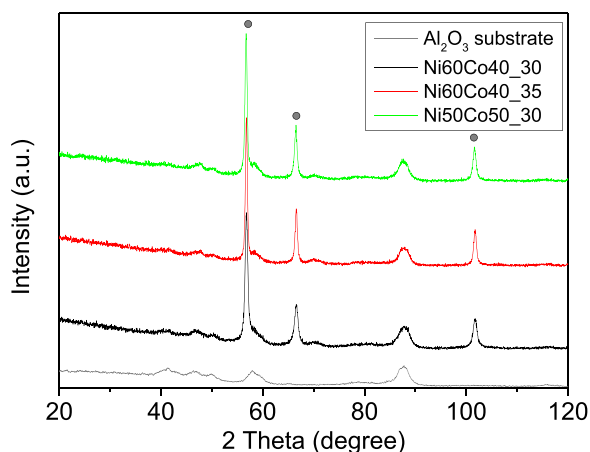

Fig. 1. X-ray diffraction pattern of supported NiCo alloys and of the bare alumina substrate that underwent the same heat treatment as the impregnated samples. Circle labels refer to the metal alloy.

Table 2
Diameter of the nanoparticles and metal dispersion D.

Sample	XRD Diameter (nm)	SEM diameter (nm)	Metal dispersion, D (%) *
$Ni_{60}Co_{40}$_30	19 ± 1	24 ± 3	4.2
$Ni_{60}Co_{40}$_35	38 ± 1	38 ± 5	2.6
$Ni_{50}Co_{50}$_30	37 ± 1	42 ± 5	2.4

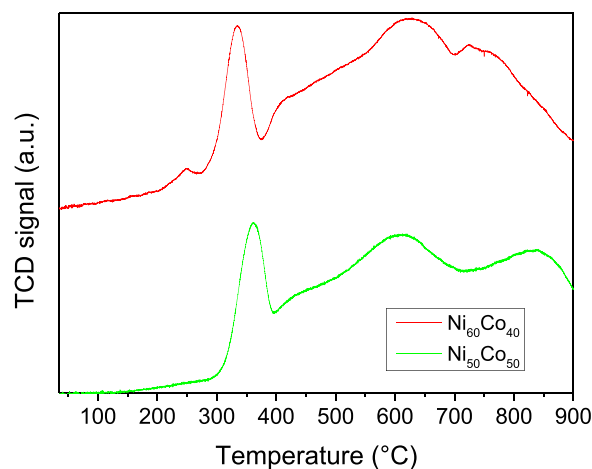* D(%) values are calculated from SEM diameter.

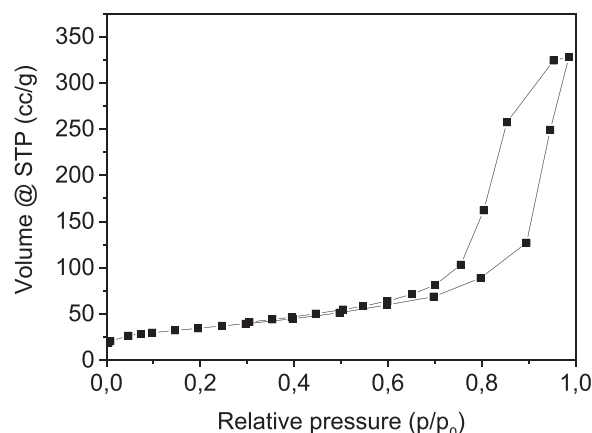**Fig. 2.** H_2-TPR profiles of $Ni_{60}Co_{40}$_30 and $Ni_{50}Co_{50}$_30 samples.

Fig. 3. Nitrogen adsorption isotherm at 77 K for the sample $Ni_{60}Co_{40}$_35.

mesoporous solids characterized by a large uptake and a broad hysteresis at high partial pressure due to the presence of a large mesoporous volume (typical of the alumina substrate). The BET surface area of the γ-Al_2O_3 support is 250 m^2/g before impregnation. Such value decreases, for the supported samples, to 146 ± 10 m^2/g ($Ni_{60}Co_{40}$_30), 171 ± 10 for ($Ni_{50}Co_{50}$_30) and 120 m^2/g ($Ni_{60}Co_{40}$_35) probably due to some mesopore occlusion by the supported metal particle. However, such drop is mainly due to thermal treatments experienced by the pellets. In fact, the specific surface area measured for the bare support that has undergone the same thermal treatments of the impregnated samples is 190 m^2/g.

SEM images are reported in Fig. 4 for the three samples and they show that nanoparticles (lighter in color dots due to their elemental composition different from that of the substrate) are always well dispersed on the substrate. The insert shows the size distribution of the metal particles. Images reported in Fig. 4b and 4c for $Ni_{60}Co_{40}$_35 and $Ni_{50}Co_{50}$_30 are very similar, showing more sparse nanoparticles
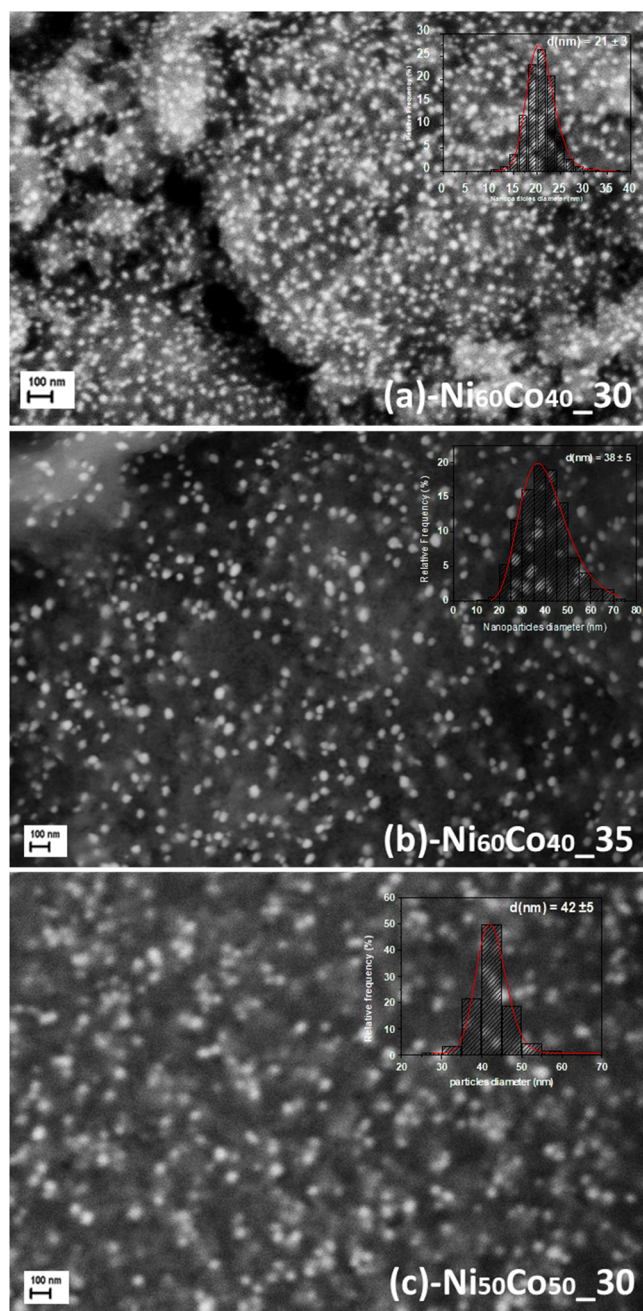
Fig. 4. SEM Images of NiCo alloys supported on γ-alumina. In (a) $Ni_{60}Co_{40}\_30$, in (b) $Ni_{60}Co_{40}\_35$ and in (c) $Ni_{50}Co_{50}\_30$.

because of their larger dimensions with respect to $Ni_{60}Co_{40}\_30\%$.

By comparison of SEM analysis and data extracted from diffraction measurements (Table 2), it is noticeable that the diameters of the nanoparticles evaluated by XRD and by microscopy are very similar, supporting the hypothesis that NiCo nanoparticles are single crystalline domain.

Increasing the concentration of salts in the synthesis process produces, as expected, samples with a higher loading and at the same time, the size of the nanoparticles grows. A comparable increase in the size of the metal nanoparticles was also observed for sample $Ni_{50}Co_{50}\_30$, although the metal loading remained constant at 30%. This phenomenon is not obvious and can be attributable to a lower interaction between metal and substrate in the samples richer in cobalt which leads to a lower dispersion of the metal on the latter. As reported in [30] the calcination process parameters (temperature, time, air flow) can be used

to modulate the final particle size distribution of the metallic alloy on the substrate.

3.1. Samples heating in absence of reaction

In Fig. 5 the Specific Absorption Rate as a function of temperature is shown for different applied fields. The maximum measured temperature is always higher than 700 °C for all samples even at low applied field of 16mT, a value considered sufficient for the sample to be tested in the reaction conditions. SAR values tend to zero at high T for all the samples.
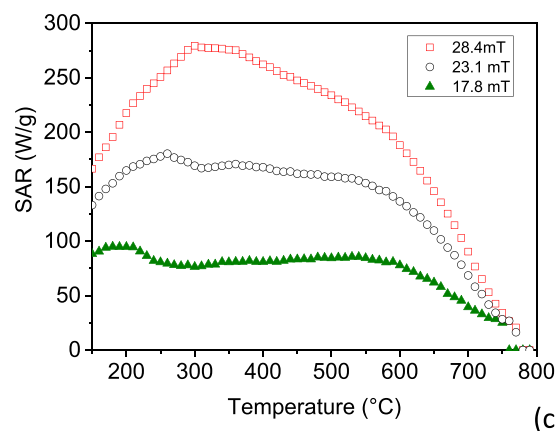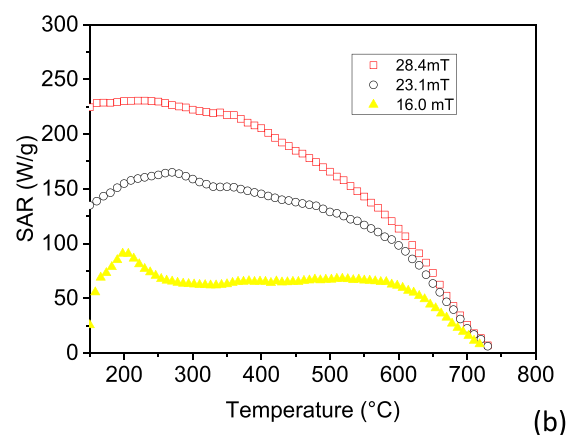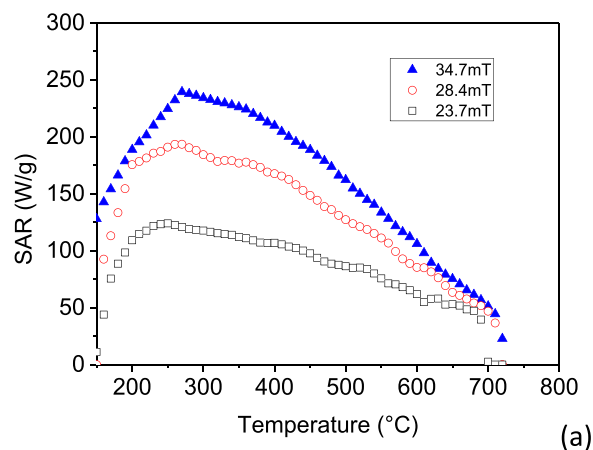

Fig. 5. Plots of calculated SAR values as a function of temperature at different field amplitudes. (a) $Ni_{60}Co_{40}\_30$, (b) $Ni_{60}Co_{40}\_35$, (c) $Ni_{50}Co_{50}\_30$. SAR has been calculated from temperature curves.

As mentioned, the maximum observable temperature limit is the Tc. In fact, hysteresis losses which constitute the main energy dissipation mechanism, rapidly vanish as temperature approaches that of magnetic ordering one (T_C). The sample $Ni_{50}CO_{50}\_30$, most likely due to its higher cobalt content, reaches the highest temperature and shows as well higher SAR values at all fields. The $Ni_{60}Co_{40}\_30$ sample shows a bell-shaped SAR trend. Specifically, at a field amplitude B of 28.4mT, SAR starts from small values at 150 °C to quickly rise with temperature until it falls off when approaching Tc. This trend, also reported in [24,42], shows that SAR does not decrease monotonously with temperature but for low field amplitudes, can also grow with temperature. Sample $Ni_{60}Co_{40}\_35$ which differs from $Ni_{60}Co_{40}\_30$ mainly with regard to mean size distribution of nanoparticles, shows a more gentle SAR decrease with temperature around Tc and the "bell" shaped trend is visible only for low amplitude field. Samples of the same composition and loading, but with larger nanoparticle sizes show significantly lower SAR values (see SI Fig. S4 and S5). The sample with higher cobalt content shows a maximum of SAR at 300 °C at 28.4mT that moves toward lower temperatures as the magnetic field decreases. Starting 600 °C SAR values rapidly decrease and as soon as temperature comes near the ordering temperature the magnetic nanoparticles are no longer able to contribute, the SAR becoming negligible as this approaches the Tc. In general, the SAR of $Ni_{50}Co_{50}\_30$ is always higher than $Ni_{60}Co_{40}$ samples and being less restricted by its Curie temperature superior temperature values are observed.

3.2. Methane reforming

As in our previous work, the chemical process of interest on which the material was tested is methane steam reforming which it is typically operated in the 700–900 °C temperature range. In a typical industrial plant, the feeding mixture CH_4/H_2O passes through a catalyst bed in tubular reactors, placed in a furnace heated from the outside by radiation/convection and conduction [43–46]. The composition of the outgoing mixture, determined mainly by the temperature, is the result of several competing or side reactions listed below.

$$CH_4 + H_2O \leftrightarrows CO + 3\,H_2$$

$$CO + H_2O \leftrightarrows CO_2 + H_2$$

$$CH_4 \leftrightarrows C + 2\,H_2$$
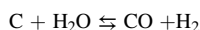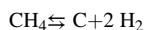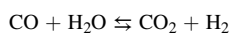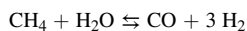
$$C + H_2O \leftrightarrows CO + H_2$$

Fig. 6 shows the reactant gas conversions and the product distribution in the gas mixture exiting the reactor for all the fresh catalyst samples that reach a specific temperature under the same applied magnetic field amplitude of 28.4 mT. All the samples need about 30 min to reach the steady state. Under the same magnetic field condition, the higher metal loading in $Ni_{60}Co_{40}\_35$ favors the attainment of higher temperatures (735 °C vs 700 °C) and conversion values (80 vs 75%) with respect to $Ni_{60}Co_{40}\_30$, as the number of dissipating agents is higher. An even higher temperature and methane conversion values (780 °C and 90%) are observed with $Ni_{50}Co_{50}\_30$ sample thanks both to a higher SAR (Fig. 3) and to a higher Curie temperature of the alloy. The result is highlighted in Fig. 7.

As the reaction temperature increases also the composition of the mixture changes. As it is possible to observe CO volume fraction raises from 13% to 15–18%. The percentage of hydrogen is quite stable since, for all the samples, temperatures above 700 °C have been recorded and, as predicted by the thermodynamic calculation, hydrogen in the mixture is rather stable (Fig. 8).

It is interesting to notice (Fig. 8) that regardless of the composition and the metal loading on the support, the measured values of hydrogen and carbon monoxide produced are in line with those expected on the basis of the thermodynamic equilibrium (continuous line in the graph).
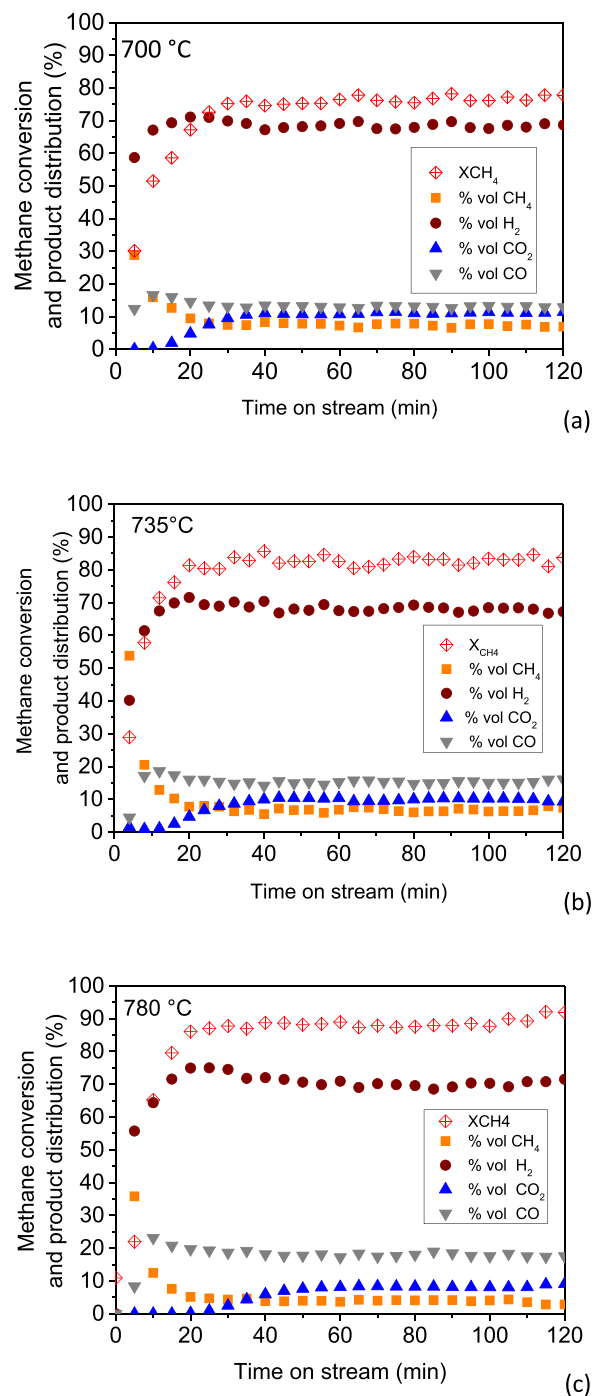

Fig. 6. Experimental product distribution and methane conversion values for sample (a) $Ni_{60}Co_{40}\_30$,(b) $Ni_{60}Co_{40}\_35$, (c) $Ni_{50}Co_{50}\_30$. Volumetric inlet flow: $N_2 = 100$ mL min^{-1}, $CH_4 = 50$ mL min^{-1}, $H_2O = 100$ mL min^{-1}. GHSV $= 3000$ h^{-1}. Applied field B $\sim$ 28,5mT. Sample: 180pellets ($\sim$5 g).

This suggests that the activity of the material is limited by the temperature that the latter is able to reach by dissipation and therefore the typical factors that govern the catalytic activity such as nanoparticles dispersion, composition, metal interaction with the substrate etc, are well and similarly optimized in the studied catalysts to let a high catalytic efficiency, near equilibrium values, for all the materials. A depression in the activity of the magnetic catalyst, expected because of the increase in the molar fraction of cobalt that is less active in the reforming reaction with respect to nickel, is not observed in this work, suggesting that surfaces of metal particles are mainly exposing Ni sites.
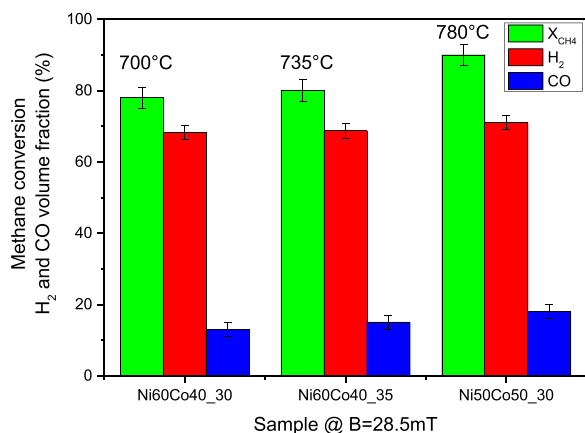
Fig. 7. Methane conversion and values of hydrogen and carbon dioxide in the outlet flow measured at B= 28.5mT for the three magnetic catalysts. The temperature reached by the samples is reported as well.
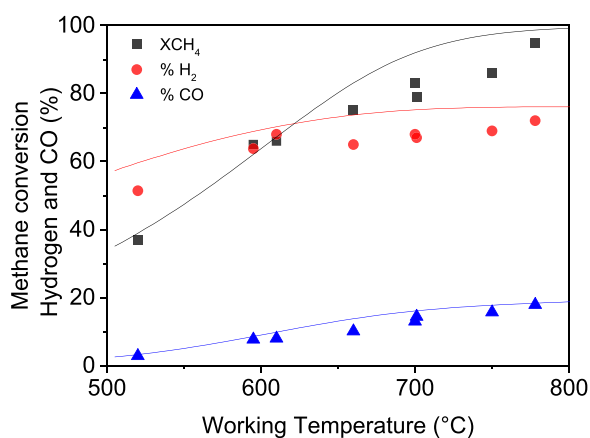

Fig. 8. Experimental methane conversion values, H_2 and CO volume fraction on a dry basis exiting the reactor as a function of the working temperature reached by induction heating, different samples. Equilibrium values calculated by HSC [47] with $CH_4:H_2O$ 1:2 mixture feed are reported as continuous lines.

The experimental methane conversion data can be discussed also in terms of the power utilized to perform the reaction. The values shown in Fig. 9 correspond to the power required to heat the catalytic bed and the feed gases to the reaction temperature and to provide the reaction heat.

An increase of the metal loading on the substrate allows to obtain slightly higher conversion values (black curve with respect to blue). Overall, $Ni_{60}Co_{40}$_30 and $Ni_{60}Co_{40}$_35 shows conversion values in the range 72–80% as a function of applied power. Such evidence is attributable to slightly higher temperatures obtained by the sample with higher metal content (for example in Fig. 7 at B=28.4mT the measured temperature on the catalyst $Ni_{60}Co_{40}$_35 is about 35 °C higher than $Ni_{60}Co_{40}$_30). On the other hand, the $Ni_{50}Co_{50}$_30 sample achieves much better conversion values than the $Ni_{60}Co_{40}$_30 sample despite the fact that cobalt is a worse catalyst than nickel. The best yields in the reforming reaction observed for the sample with the highest cobalt content are attributable to its better heating ability (SAR) which, at the same power, allows the achievement of higher temperatures.

The figure reiterates the role played by the working temperature that can be reached during the inductive process on the observed conversion and the necessity in magnetic catalysis to optimize the SAR of dissipating agents.
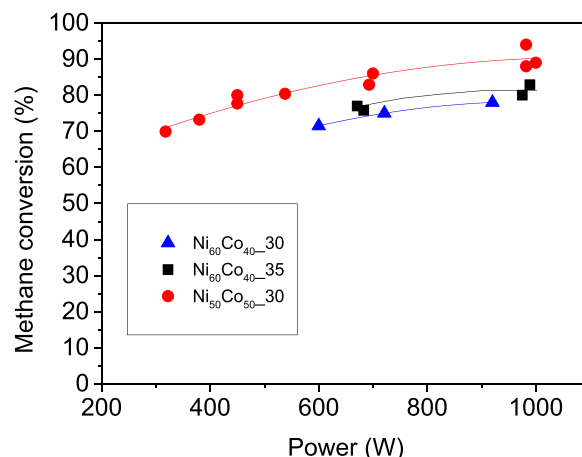

Fig. 9. Methane conversion as a function of the power delivered to the inductor. Total gas flow:250 mL/min. Amount of catalyst: 180 γ-Al_2O_3 pellets loaded with NiCo alloy (~5 g). GHSV= 3000 h^{-1}.

4. Conclusions

NiCo supported magnetic catalysts having different total metal loading and metal molar ratio have been synthesized using a traditional impregnation procedure and characterized in terms of morphological and structural properties. All the produced samples, despite the consistent metallic loading, show well dispersed alloy nanoparticles. Supported NiCo catalysts are able to catalyze the methane steam reforming reaction powered by induction heating reaching methane conversion and syngas yields close to expected equilibrium values at all applied powers.

The catalyst's ability of dissipating an external radio frequency electromagnetic field has been explored evaluating the temperature heating and cooling curves. We have shown that the methane conversion value in the steam reforming reaction can be improved by increasing the total amount of cobalt in the alloy.

Both explored strategies, increasing total metal loading and increasing the amount of cobalt in the alloy, were found to be effective in achieving higher operating temperatures than previously developed materials. In particular, the induction heating of the alloy with the highest cobalt content, allows to observe higher methane conversion values, minimizing the energy required to feed the reaction.

The developed magnetic catalysts contribute to the transition to distributed hydrogen production and help to tackle some of the challenges related to the intensification of production processes by electrification.

CRediT authorship contribution statement

Violetta Poletto Dotsenko: Investigation, Formal Analysis, **Mariangela Bellusci:** Conceptualization, Formal analysis, Writing, **AndreaMasi:** Investigation, Formal analysis, **Daniela Pietrogiacomi:** Formal analysis, **Francesca Varsano:** Conceptualization, Formal analysis, Supervision, Writing - original draft, Writing - review & editing.

Declaration of Competing Interest

The authors declare that they have no known competing financial interests or personal relationships that could have appeared to influence the work reported in this paper.

Data Availability

Data will be made available on request.

Acknowledgements

This work was supported by ENEA within the program POC2020, project MAGNETICAT.

Appendix A. Supporting information

Supplementary data associated with this article can be found in the online version at doi:10.1016/j.cattod.2023.114049.

References

[1] Z.J. Schiffer, K. Manthiram, Electrification and decarbonization of the chemical industry, Joule 1 (2017) 10–14, https://doi.org/10.1016/j.joule.2017.07.008.

[2] G. Centi, S. Perathoner, Status and gaps toward fossil-free sustainable chemical production, Green Chem. 24 (2022) 7305–7331, https://doi.org/10.1039/D2GC01572B.

[3] K.M. Van Geem, B.M. Weckhuysen, Toward an e-chemistree: materials for electrification of the chemical industry, MRS Bull. 46 (2021) 1187–1196, https://doi.org/10.1557/s43577-021-00247-5.

[4] I. Eryazici, N. Ramesh, C. Villa, Electrification of the chemical industry—materials innovations for a lower carbon future, MRS Bull. 46 (2021) 1197–1204, https://doi.org/10.1557/s43577-021-00243-9.

[5] M. Ambrosetti, A perspective on power-to-heat in catalytic processes for decarbonization, Chem. Eng. Process. - Process. Intensif. 182 (2022), 109187, https://doi.org/10.1016/j.cep.2022.109187.

[6] S.T. Wismann, J.S. Engbæk, S.B. Vendelbo, F.B. Bendixen, W.L. Eriksen, K. Aasberg-Petersen, C. Frandsen, I. Chorkendorff, P.M. Mortensen, Electrified methane reforming: a compact approach to greener industrial hydrogen production, Science 364 (2019) 756–759, https://doi.org/10.1126/science.aaw8775.

[7] Q. Dong, Y. Yao, S. Cheng, K. Alexopoulos, J. Gao, S. Srinivas, Y. Wang, Y. Pei, C. Zheng, A.H. Brozena, H. Zhao, X. Wang, H.E. Toraman, B. Yang, I.G. Kevrekidis, Y. Ju, D.G. Vlachos, D. Liu, L. Hu, Programmable heating and quenching for efficient thermochemical synthesis, Nature 605 (2022) 470–476, https://doi.org/10.1038/s41586-022-04568-6.

[8] G.B. Marin, K.M. Van Geem, Electrified temperature-modulated synthesis, Nat. Synth. 1 (2022) 512–513, https://doi.org/10.1038/s44160-022-00112-6.

[9] M. Ambrosetti, A. Beretta, G. Groppi, E. Tronconi, A numerical investigation of electrically-heated methane steam reforming over structured catalysts, Front. Chem. Eng. 3 (2021), https://doi.org/10.3389/fceng.2021.747636.

[10] L. Zheng, M. Ambrosetti, D. Marangoni, A. Beretta, G. Groppi, E. Tronconi, Electrified methane steam reforming on a washcoated <scp>SiSiC</scp> foam for low-carbon hydrogen production, AIChE J. (2022), https://doi.org/10.1002/aic.17620.

[11] E. Meloni, M. Martino, V. Palma, Microwave assisted steam reforming in a high efficiency catalytic reactor, Renew. Energy 197 (2022) 893–901, https://doi.org/10.1016/j.renene.2022.07.157.

[12] E. Meloni, M. Martino, A. Ricca, V. Palma, Ultracompact methane steam reforming reactor based on microwaves susceptible structured catalysts for distributed hydrogen production, Int J. Hydrog. Energy 46 (2021) 13729–13747, https://doi.org/10.1016/j.ijhydene.2020.06.299.

[13] S. Hamzehlouia, S.A. Jaffer, J. Chaouki, Microwave heating-assisted catalytic dry reforming of methane to syngas, Sci. Rep. 8 (2018) 8940, https://doi.org/10.1038/s41598-018-27381-6.

[14] H.M. Nguyen, G.H. Pham, R. Ran, R. Vagnoni, V. Pareek, S. Liu, Dry reforming of methane over Co–Mo/Al 2 O 3 catalyst under low microwave power irradiation, Catal. Sci. Technol. 8 (2018) 5315–5324, https://doi.org/10.1039/C8CY01601A.

[15] B. Fidalgo, J.A. Menéndez, Study of energy consumption in a laboratory pilot plant for the microwave-assisted CO2 reforming of CH4, Fuel Process. Technol. 95 (2012) 55–61, https://doi.org/10.1016/j.fuproc.2011.11.012.

[16] C. Kuhwald, S. Türkhan, A. Kirschning, Inductive heating and flow chemistry – a perfect synergy of emerging enabling technologies, Beilstein J. Org. Chem. 18 (2022) 688–706, https://doi.org/10.3762/bjoc.18.70.

[17] S. Ceylan, C. Friese, C. Lammel, K. Mazac, A. Kirschning, Inductive heating for organic synthesis by using functionalized magnetic nanoparticles inside microreactors, Angew. Chem. Int. Ed. 47 (2008) 8950–8953, https://doi.org/10.1002/anie.200801474.

[18] T.K. Houlding, E.V. Rebrov, Application of alternative energy forms in catalytic reactor engineering, Green. Process. Synth. 1 (2012) 19–31, https://doi.org/10.1515/greenps-2011-0502.

[19] A. Bordet, L.-M. Lacroix, P.-F. Fazzini, J. Carrey, K. Soulantica, B. Chaudret, Magnetically induced continuous cO 2 hydrogenation using composite iron carbide nanoparticles of exceptionally high heating power, Angew. Chem. 128 (2016) 16126–16130, https://doi.org/10.1002/ange.201609477.

[20] M.G. Vinum, M.R. Almind, J.S. Engbæk, S.B. Vendelbo, M.F. Hansen, C. Frandsen, J. Bendix, P.M. Mortensen, Dual-function cobalt–nickel nanoparticles tailored for high-temperature induction-heated steam methane reforming, Angew. Chem. Int. Ed. 57 (2018) 10569–10573, https://doi.org/10.1002/anie.201804832.

[21] M. Bellusci, A. Masi, M. Albino, D. Peddis, M. Petrecca, C. Sangregorio, A. La Barbera, F. Varsano, Fe<inf>3</inf>O<inf>4</inf>@HKUST-1 magnetic composites by mechanochemical route for induction triggered release of carbon

[22] M.N. Pérez-Camacho, J. Abu-Dahrieh, D. Rooney, K. Sun, Biogas reforming using renewable wind energy and induction heating, Catal. Today 242 (2015) 129–138, https://doi.org/10.1016/j.cattod.2014.06.010.

[23] H.M. Nguyen, C.M. Phan, S. Liu, C. Pham-Huu, L. Nguyen-Dinh, Radio-frequency induction heating powered low-temperature catalytic CO2 conversion via bi-reforming of methane, Chem. Eng. J. 430 (2022), 132934, https://doi.org/10.1016/j.cej.2021.132934.

[24] M.R. Almind, M.G. Vinum, S.T. Wismann, M.F. Hansen, S.B. Vendelbo, J.S. Engbæk, P.M. Mortensen, I. Chorkendorff, C. Frandsen, Optimized CoNi nanoparticle composition for curie-temperature-controlled induction-heated catalysis, ACS Appl. Nano Mater. 4 (2021) 11537–11544, https://doi.org/10.1021/acsanm.1c01941.

[25] F. Wang, D. Guan, Y. Li, J. Zhong, Research progress on magnetic catalysts and its application in hydrogen production area, Energ. (Basel) 15 (2022) 5327, https://doi.org/10.3390/en15155327.

[26] J. Marbaix, N. Mille, L.-M. Lacroix, J.M. Asensio, P.-F. Fazzini, K. Soulantica, J. Carrey, B. Chaudret, Tuning the composition of FeCo nanoparticle heating agents for magnetically induced catalysis, ACS Appl. Nano Mater. 3 (2020) 3767–3778, https://doi.org/10.1021/acsanm.0c00444.

[27] W. Wang, G. Tuci, C. Duong-Viet, Y. Liu, A. Rossin, L. Luconi, J.-M. Nhut, L. Nguyen-Dinh, C. Pham-Huu, G. Giambastiani, Induction heating: an enabling technology for the heat management in catalytic processes, ACS Catal. 9 (2019) 7921–7935, https://doi.org/10.1021/acscatal.9b02471.

[28] A. Hart, M. Adam, J.P. Robinson, S.P. Rigby, J. Wood, Inductive heating assisted-catalytic dehydrogenation of tetralin as a hydrogen source for downhole catalytic upgrading of heavy oil, Top. Catal. 63 (2020) 268–280, https://doi.org/10.1007/s11244-019-01206-w.

[29] A. Zadražil, F. Štěpánek, Remote control of reaction rate by radiofrequency heating of composite catalyst pellets, Chem. Eng. Sci. 134 (2015) 721–726, https://doi.org/10.1016/j.ces.2015.05.055.

[30] C. Scarfiello, M. Bellusci, L. Pilloni, D. Pietrogiacomi, A. La Barbera, F. Varsano, Supported catalysts for induction-heated steam reforming of methane, Int J. Hydrog. Energy 46 (2021) 134–145, https://doi.org/10.1016/j.ijhydene.2020.09.262.

[31] L.K.T.B. Massalski, H. Okamoto, P.R. Subramanian (Eds.), Binary Alloy Phase Diagrams, 2nd ed.,, ASM International, Metals Park Ohio, 1990.

[32] P. van Helden, F. Prinsloo, J.-A. van den Berg, B. Xaba, W. Erasmus, M. Claeys, J. van de Loosdrecht, Cobalt-nickel bimetallic Fischer-Tropsch catalysts: A combined theoretical and experimental approach, Catal. Today 342 (2020) 88–98, https://doi.org/10.1016/j.cattod.2019.03.001.

[33] C.A. Schneider, W.S. Rasband, K.W. Eliceiri, NIH Image to ImageJ: 25 years of image analysis, Nat. Methods 9 (2012) 671–675, https://doi.org/10.1038/nmeth.2089.

[34] F. Varsano, M. Bellusci, A. La Barbera, M. Petrecca, M. Albino, C. Sangregorio, Dry reforming of methane powered by magnetic induction, Int J. Hydrog. Energy 44 (2019) 21037–21044, https://doi.org/10.1016/j.ijhydene.2019.02.055.

[35] N. Mille, S. Faure, M. Estrader, D. Yi, J. Marbaix, D. De Masi, K. Soulantica, A. Millán, B. Chaudret, J. Carrey, A setup to measure the temperature-dependent heating power of magnetically heated nanoparticles up to high temperature, Rev. Sci. Instrum. 92 (2021), 054905, https://doi.org/10.1063/5.0038912.

[36] H. Kreissl, J. Jin, S. Lin, D. Schüette, S. Störtte, N. Levin, B. Chaudret, A.J. Vorholt, A. Bordet, W. Leitner, Commercial Cu 2 Cr 2 O 5 decorated with iron carbide nanoparticles as a multifunctional catalyst for magnetically induced continuous-flow hydrogenation of aromatic ketones, Angew. Chem. Int. Ed. 60 (2021) 26639–26646, https://doi.org/10.1002/anie.202107916.

[37] J.M. Asensio, A.B. Miguel, P. Fazzini, P.W.N.M. vanLeeuwen, B. Chaudret, Hydrodeoxygenation using magnetic induction: high-temperature heterogeneous catalysis in solution, Angew. Chem. Int. Ed. 58 (2019) 11306–11310, https://doi.org/10.1002/anie.201904366.

[38] K. Shimura, T. Miyazawa, T. Hanaoka, S. Hirata, Tropsch synthesis over alumina supported bimetallic Co – Ni catalyst: Effect of impregnation sequence and solution, J. Mol. Catal. Fisch. 407 (2015) 15–24.

[39] X. Zhao, G. Lu, Modulating and controlling active species dispersion over Ni–Co bimetallic catalysts for enhancement of hydrogen production of ethanol steam reforming, Int J. Hydrog. Energy 41 (2016) 3349–3362, https://doi.org/10.1016/j.ijhydene.2015.09.063.

[40] E. Rytter, T.H. Skagseth, S. Eri, A.O. Sjåstad, Tropsch catalysts using nickel promoter as a rhenium substitute to suppress deactivation, Cobalt Fisch. (2010) 4140–4148.

[41] K. Shimura, T. Miyazawa, T. Hanaoka, S. Hirata, Journal of molecular catalysis a: chemical fischer – tropsch synthesis over alumina supported bimetallic Co – Ni catalyst: Effect of impregnation sequence and solution, J. Mol. Catal. A Chem. 407 (2015) 15–24, https://doi.org/10.1016/j.molcata.2015.06.013.

[42] Z. Nemati, J. Alonso, I. Rodrigo, R. Das, E. Garaio, J.Á. García, I. Orue, M.H. Phan, H. Srikanth, Improving the heating efficiency of iron oxide nanoparticles by tuning their shape and size, J. Phys. Chem. C 122 (2018) 2367–2381, https://doi.org/10.1021/acs.jpcc.7b10528.

[43] R.M. Navarro, M.A. Peña, J.L.G. Fierro, Hydrogen production reactions from carbon feedstocks: fossil fuels and biomass, Chem. Rev. 107 (2007) 3952–3991, https://doi.org/10.1021/cr0501994.

[44] Z. Wei, J. Sun, Y. Li, A.K. Datye, Y. Wang, Bimetallic catalysts for hydrogen generation, Chem. Soc. Rev. 41 (2012) 7994, https://doi.org/10.1039/c2cs35201j.

[45] T.L. LeValley, A.R. Richard, M. Fan, The progress in water gas shift and steam reforming hydrogen production technologies – A review, Int J. Hydrog. Energy 39 (2014) 16983–17000, https://doi.org/10.1016/j.ijhydene.2014.08.041.

[46] E. Meloni, M. Martino, V. Palma, A short review on ni based catalysts and related engineering issues for methane steam reforming, Catalysts 10 (2020) 352, https://doi.org/10.3390/catal10030352.

[47] Outokumpu research, No Title HSC Chemistry 6.12, (n.d.).